

Article

An Integrated Petrographic, Geomatic and Geophysical Approach for the Characterization of the Carbonate Rocks of the Calcari di Cagliari Formation

Giuseppe Casula ^{1,*}, Silvana Fais ^{2,3,4}, Francesco Cuccuru ², Maria Giovanna Bianchi ¹ and Paola Ligas ²

¹ Istituto Nazionale di Geofisica e Vulcanologia (INGV)—Sezione di Bologna, Viale Berti Pichat 6/2, 40127 Bologna, Italy; mariagiovanna.bianchi@ingv.it

² Department of Civil, Environmental Engineering and Architecture (DICAAR), University of Cagliari, Via Marengo 2, 09123 Cagliari, Italy; sfais@unica.it (S.F.); cuccuru.f@gmail.com (F.C.); pligas@unica.it (P.L.)

³ Consorzio Interuniversitario Nazionale per l'Ingegneria delle Georisorse, CINIGEO, Palazzo Baleani, Corso Vittorio Emanuele II 244, 00186 Roma, Italy

⁴ National Research Council of Italy (CNR)—Institute of Environmental Geology and Geoengineering (IGAG), Via Marengo 2, 09123 Cagliari, Italy

* Correspondence: giuseppe.casula@ingv.it; Tel.: +39-0514151415

Abstract: Non-invasive techniques, such as close-range photogrammetry (CRP) and 3D ultrasonic tomography complemented with optical and scanning electron microscopy and mercury porosimetry, were applied to characterize the carbonate rock samples of the Calcari di Cagliari formation. The integrated approach started with the computation of high-resolution 3D models of the carbonate samples using the CRP technique to produce 3D high-resolution models texturized both with natural colors and intensity. Starting from the 3D models from previous techniques, a 3D ultrasonic tomography on each rock sample was accurately planned and carried out in order to detect the elastic properties of such rocks and relate them to textural heterogeneity or internal defects. The results indicate that the relationship between longitudinal velocity and rock properties is complex even in the same carbonate formation. Understanding the relationship between the geomatic and geophysical responses in the investigated rock properties, such as textural characteristics and especially structure and geometry of pores, type of pores, tortuosity and cementing material, is important for many practical applications and especially in the diagnostic process of the conservation state of monumental structures. The integration of the above non-invasive techniques complemented by petrographical–petrophysical data proved to be a powerful method to associate each lithotype with a different susceptibility to degradation. The results presented in this paper demonstrate that the proposed integrated use of complementary methodologies would guarantee the reproducibility of the measurements both at the laboratory and field scale for the monitoring in time of the rock condition while giving a useful contribution in making decisions on an appropriate remedial strategy.

Keywords: carbonate rocks; petrographic data; photogrammetry; ultrasonic tomography; integrated interpretation



Citation: Casula, G.; Fais, S.; Cuccuru, F.; Bianchi, M.G.; Ligas, P. An Integrated Petrographic, Geomatic and Geophysical Approach for the Characterization of the Carbonate Rocks of the Calcari di Cagliari Formation. *Minerals* **2024**, *14*, 501. <https://doi.org/10.3390/min14050501>

Academic Editors: Daniele Moro and Adrián Durán Benito

Received: 29 February 2024

Revised: 26 April 2024

Accepted: 6 May 2024

Published: 10 May 2024



Copyright: © 2024 by the authors. Licensee MDPI, Basel, Switzerland. This article is an open access article distributed under the terms and conditions of the Creative Commons Attribution (CC BY) license (<https://creativecommons.org/licenses/by/4.0/>).

1. Introduction

This paper focuses on the integrated application of geomatic and geophysical non-invasive techniques integrated with petrographical data for the experimental characterization of significant samples of carbonate rocks known as the Calcari di Cagliari formation. The integration of all data aimed to provide a better understanding of the possibility of disintegration and alteration involving the Calcari di Cagliari, and ultimately for the prevention and conservation of buildings of historical and artistic interest. In fact, most of the buildings in the historic center of the town of Cagliari were built using the above carbonate materials, which are comparable to other carbonate building materials used in the Mediterranean Basin in both construction and ornamentation [1–6].

Traditionally the characterization of carbonate materials has been carried out using optical microscopy (OM) and scanning electron microscopy (SEM) to analyze thin sections appropriately prepared from specimens [7–11]. Though indispensable for the important information provided, this approach is clearly destructive and there is a limit to the number of samples that can be lost. Furthermore, using traditional petrographic techniques alone, we cannot analyze the evolving processes of degradation by observing the shallow and in-depth conditions of the stone materials in time. In recent years, the use of non-invasive techniques has been developed in many fields of applied research [12–15] and especially in the analysis of stone materials [2,16–22]. Furthermore, non-invasive techniques are the most appropriate for assessing the quality of stone building materials in monumental and historic structures. For a successful on-site analysis, it is crucial to carry out a non-invasive characterization of samples from the same quarries of origin as the construction materials.

As is known, the non-invasive analysis of rock samples is becoming ever more widespread with the introduction of high-tech methods, such as X-ray computed tomography (X-ray CT), X-ray micro-computed tomography (X-ray micro-CT), digital radiography, micro X-ray fluorescence (μ -XRF) [23–25] and others. X-ray CT is a very effective non-destructive method for providing the three-dimensional structures of rock core samples [26] or complex artworks [27,28]. X-ray micro-CT and digital radiography are non-destructive techniques that provide high-resolution images of the internal structures of the investigated stone materials. In addition, micro-CT images can be elaborated for the realization of high-resolution 3D digital reconstructions and models. These high-tech methods provide a great amount of microstructural information. Furthermore, these high-tech methods are extensively used in hydrocarbon research to analyze the porous structure of rock samples, and in scientific drilling to help the interpretation of lithology and structure while preserving the digital record of the core prior to sacrificing it for subsequent destructive analyses [29–31]. Some degradation areas inside the materials can be also detected by means of neutron diffraction [32] and neutron tomography [33,34]. However, the above recent techniques involve very expensive equipment available in few technologically advanced laboratories.

In this study we have chosen to apply an integrated petrographic, geomatic and geophysical approach for stone material characterization to provide accurate, fast and reliable results at a resolution suitable for the preset scientific targets, but at the same time more accessible and at low cost, thus making it available for technicians working in the cultural heritage field.

Nowadays, among the geomatic methodologies used to compute high spatial resolution 3D models of objects of complex shapes, close-range photogrammetry (CRP) based on structure from motion (SfM) and multi view stereo matching (MVS) algorithms derived from computer vision are actually some of the most used methods in different fields of geomatics like terrain surface modeling, digital elevation modeling (DEM), digital terrain modeling (DTM), digital surface model (DSM) computations, architectural, historical and modern building information modeling (BIM) and so on [35,36]. In fact, SfM-based techniques have already proven to be successful for accurate 3D modeling of built structures, bare geological substrates and fine spatial scale individual plant structures [37,38]. This methodology can produce 3D models with properties similar to those of laser imaging detection and ranging (LIDAR), but with red–green–blue (RGB) spectral attributes for each point of the surface of the analyzed targets [39]. The technique consists essentially of the computation of high-resolution point clouds and corresponding meshes texturized with natural colors based on the inherent motion of numerous overlapping images taken from different locations, in particular arrays of good quality 2D images like photographs acquired with optical cameras in the terrestrial modality as well as in the aerial one with the aid of low-cost unmanned aerial vehicles (UAV). The terrestrial modality is used when high-resolution and performant optical cameras that are too heavy and bulky to be mounted on drones must be used; conversely, aerial surveys are used when parts of a studied complex-shaped object, like building roofs or areas of terrains of difficult access, are unreachable from the ground [39]. In this work, we used a low-cost commercial grade digital camera to

compute high spatial resolution 3D models of significant samples of carbonate facies of the Calcarei di Cagliari.

The above geomatic technique is very useful to analyze shallow parts of the stone materials and holds vast potential for improving both the quality and efficiency of a 3D digital model useful for the subsequent geophysical analyses. In fact, the high-resolution (HR) 3D models of the investigated carbonate samples have provided accurate information on their geometrical shape, for example, the presence of defects, small cavities of different origins, fractures and alteration zones in the shallow part of the investigated materials.

Geophysical techniques, such as the ultrasonic tomography applied in this study, can detect the elasto-mechanical conditions inside the materials while analyzing the propagation of elastic waves within them. The knowledge of the elastic properties of the carbonate rocks is quite challenging due to their heterogeneity and complexity.

Many researchers [18,22,40–45] have studied the relations between the longitudinal and/or transverse velocities with petrographic and petrophysical characteristics of the carbonate materials, using laboratory techniques based on the ultrasonic velocity test. An accurate petrographic study using optical and electronic microscopy can improve the interpretation of the non-invasive diagnostic techniques, and especially the deep understanding of the behavior of the ultrasonic signal propagation [9,46–51].

The advantage of the ultrasonic method is that it is easy to use, less costly and non-destructive. Furthermore, it can be used both in the laboratory and in the field and proves useful in many sectors of the applied research. In this study, we carried out a laboratory ultrasonic survey at a resonance frequency of 82 kHz by acquiring and processing 3D ultrasonic travel-time tomography data (namely P-wave travel times) on the significant samples of the Calcarei di Cagliari formation. Three-dimensional ultrasonic tomography (3D UT) represents a high-resolution technique to inspect the inner parts of the investigated rock samples providing information on their elastic properties variations related to their petrophysical and mechanical properties. In planning and interpreting the 3D UT, the above geomatic techniques play an extremely important role, since they provide high-resolution 3D digital models to precisely locate a large quantity of measurements (e.g., locations of the ultrasonic signal transmission and receiver points). Furthermore, the 3D digital model obtained by SfM photogrammetry also represents an effective tool for the accurate and effective representation of the 3D tomographic results, allowing the precise locations of longitudinal velocity changes in relation to the textural variation of the materials and the presence of defects or altered zones inside them.

Taking into account the aspects considered above, the aim of this paper was to provide a framework for the applicability of some non-destructive techniques (NDT) supported by OM and SEM observations of thin sections cut from the same samples used for the non-destructive characterization. The OM and SEM have also been complemented by mercury intrusion porosimetry (MIP) to obtain further information on the structure of the porosity system of the investigated carbonate rocks.

2. Materials and Methods

2.1. Materials

The carbonate succession known as Calcarei di Cagliari outcrops in the hills and along the coast of the city of Cagliari [52,53].

The late Miocene transgressive succession of the Calcarei di Cagliari is characterized by a basal part in which Tortonian carbonate sediments (mudstones and wackestones) of an external platform have been deposited. With the progressive decreasing bathymetry that occurred in the upper Tortonian–lower Messinian, biogenic carbonate platforms of the littoral environment developed. The change in the sedimentation environment due to bathymetric variations led to three distinct carbonate facies, named from bottom to top, Pietra Cantone, Tramezzario and Pietra Forte. These were the names given to these lithotypes by the old quarrymen.

The Pietra Cantone is a yellow, poorly stratified, bioclastic limestone with a mud-supported texture due to a carbonate sedimentation that occurred at a paleobathymetry of about 60–80 m, belonging to the circalittoral plane [54]. This rock is characterized by a high content of planktonic and benthic foraminifera, and small amounts of iron oxides and terrigenous components such as quartz, feldspars and biotite. The fossiliferous content has allowed us to date this lithotype to the Tortonian age [52,55].

The Tramezzario is a white bioclastic limestone with a grain-supported (grainstone-packstone) texture, characterized by a textural heterogeneity with both reef facies rich in bioclasts and deeper sea facies rich in carbonate mud. However, the biocenoses that characterize the Tramezzario indicate a paleobathymetry of sedimentation not exceeding 40 m, belonging to the infralittoral–circalittoral bathymetric plane [54]. Isotope analyses performed with the $^{86}\text{Sr}/^{87}\text{Sr}$ method have provided an age referable to the end of the Tortonian [56].

The Miocene carbonate succession of the Calcari di Cagliari ends with the Pietra Forte, a cream-colored biohermal or biostromal massive limestone, typical of a littoral–infralittoral depositional environment with high energy and a paleobathymetry less than 30 m [54]. The deposition of the Pietra Forte is mainly due to the growth of *Lithothamnium* algae in which bioclasts of a different nature were incorporated, mainly bivalves, gastropods, crustaceans and colonies of bryozoans. Based on the faunas and the stratigraphic position, the Pietra Forte can be dated back to the Tortonian, but due to some affinity with similar formations in the Gulf of Oristano (Sardinia, Italy) it can also be referred to the Messinian [54,55].

The different intrinsic characteristics of each limestone facies affect the forms and intensity of degradation. Pietra Cantone is a poorly cemented rock, characterized by a microporous carbonate matrix which makes it hygroscopic and therefore susceptible to aggressive forms of decay such as alveolization (Figure 1a). The outcrops and artefacts made up of this lithotype are more susceptible than the other two lithotypes of the Calcari di Cagliari formation to degradation due to salt-rich aerosols from the sea. The saline solution permeates deeply into the rock and when the salts crystallize, they cause micro-fractures and a loss of material in the form of dust. The Tramezzario is usually a hard, compact rock, although in several cases it is characterized by the combination of weak cementation and high secondary porosity that can cause severe degradation forms. In particular conditions, such as high moisture levels, degradation occurs more intensely, causing detachment and the complete disintegration of the rock into carbonate mud (powder) (Figure 1b).

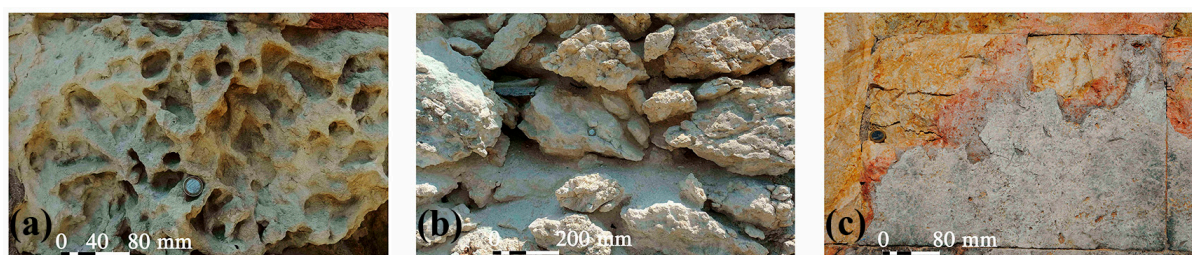


Figure 1. Degradation forms of the Calcari di Cagliari limestones: (a) alveolization of the Pietra Cantone; (b) loss of material and pulverization in a wall built with Tramezzario ashlar; (c) detachment and oxidation in a Pietra Forte ashlar.

The Pietra Forte is generally a very compact, tenacious and hard limestone. Due to its excellent cementation, it is less susceptible to decay. However, fractures, detachments and oxidation could affect this lithotype (Figure 1c). Fractures are often caused by stress exceeding the rock's strength that causes a loss of cohesion along the weakest planes of the rock. The detachment of material is generally due to the release of inner tensions after the rock is quarried and reduced to ashlar for building. Especially within the fractures, the Pietra Forte can present impurities containing iron minerals which, by oxidation, create red-brown patinas that render the altered material brittle and favor its detachment. The Pietra Forte is also affected by dissolution phenomena that produce macropores and superficial

and hypogenic karst forms. The karst forms can be large and can extend over wide areas, making the Pietra Forte the main aquifer of the city of Cagliari.

2.2. Optical and Scanning Electron Microscopy

Thin sections of the three facies of Calcari di Cagliari were analyzed by optical microscopy (OM) and scanning electron microscopy (SEM) in order to identify their textural characteristics and the amount and type of pores, in particular micropores by SEM. OM analysis was carried out by means of a petrographic microscope in polarized light (Carl Zeiss Axioplan microscope—Carl Zeiss, Oberkochen, Germany). SEM was carried out by a Zeiss EVO 50 VP model scanning electron microscope (Carl Zeiss, Oberkochen, Germany) connected to an EDS X-Max (Oxford Analytical Instruments Ltd., High Wycombe, UK). SEM was performed under a high vacuum with an electron high tension (EHT) of 20 kV, a working distance (WD) of 10 mm, an Iprobe current of 200 pA, and a resolution of about 1–2 nm. The thin sections studied with OM were treated with blue dye epoxy resin to better visualize the pore space [22,48,57,58] and their connection at the meso-scale [59], while for SEM, the thin sections were metal-coated, creating a conductive 10 nm layer of gold on their surfaces to inhibit charging, reduce thermal damage and improve the secondary electron signal required for the morphology examination.

2.3. Mercury Intrusion Porosimetry

The knowledge on the textural features of the Calcari di Cagliari by OM and SEM was implemented with quantitative information on the pore structures obtained by the mercury intrusion porosimetry (MIP) technique. Fifteen cubic representative samples (with the largest dimension of 1.5 cm per side), five from each carbonate lithotype (Pietra Cantone, Tramezzario and Pietra Forte), were prepared and dried in an oven at 60 °C for 48 h for the MIP analyses. A Micromeritics Autopore IV 9500 (Micromeritics Instrument Corporation, Norcross, GA, USA) was used to measure the connected porosity for pore-throat diameters that cover the 3 nm–360 µm range, applying an initial pressure of 0.5 psia and reaching a maximum pressure of 60,000 psia to measure the smallest pore-throat diameters. Owing to MIP analyses, it was possible to quantify the number of connected pores (effective porosity), pore-throat size distributions (radii/diameters) and bulk and skeletal densities. Besides this information, some key petrophysical parameters of the pore network, such as permeability and tortuosity [60–62], were deduced. These parameters depend on the size and arrangement of pores/throats and pore-to-pore connections. Mercury intrusion porosimeter instruments can compute permeability and tortuosity using their specialist software by applying the well-known relationship proposed by Katz and Thompson [59,60], who introduced the K-T method to calculate permeability, and by Hager [61], who proposed a relationship for the calculation of tortuosity.

2.4. CRP Method

Data Acquisition—Three prismatic-shaped significative samples of each investigated lithotype, namely, Pietra Cantone, Tramezzario and Pietra Forte, of the Calcari di Cagliari formation were prepared with an average volume of about $20 \times 10 \times 10 \text{ cm}^3$. Two terrestrial photogrammetric campaigns were performed on two different days in this study: 30 December 2022 and 2 January 2023. A single lens commercial digital camera model, namely the Canon Power Shot 730 HS CMOS with a resolution of 20.3 Mpx, was operated to acquire sets of about a hundred high-quality 2D photo images for every rock sample, all around the samples under study, at short and predetermined distances (20–50 cm) and at different station points evenly spaced at a mean distance of 10 cm between them (about 80% overlapping). Finally, all images were collected under light conditions as homogeneous as possible and after positioning the studied sample on a calibrated base equipped with reference markers characterized by high reflectivity contrast and known dimensions [9,18,42].

Data Processing—At the pre-processing stage, the 2D images were first manually trimmed to remove unusable photos; they were then pre-processed with release 2.0.2 of the AgisoftMetashape[®] software (Agisoft LLC, St. Petersburg, Russia) based on structure from motion (SfM) methodology to avoid the use of noisy data, to finely align poses and to generate a highly dense point cloud.

Image alignment and sparse cloud generation—At the image orientation stage, the position of the camera is detected, the photo orientation is determined using both intrinsic camera parameters, such as focal length, coordinates of the image principal point and lens distortion coefficients, and extrinsic orientation parameters, such as the three translation components and the three Euler rotation angles estimated during the image orientation process. After the image orientation procedure is successfully completed, an a priori model in the form of a discrete point cloud is generated using essentially the reference points [63].

Dense cloud generation, meshing and texturing—At the following stage of dense cloud generation, a multi view stereo matching (MVS)-styled process is started, by which depth maps are calculated to perform the densification of points. The depth maps are computed essentially using the image pairs that overlap and taking into account the intrinsic and extrinsic orientation parameters derived from the bundle adjustment operations.

A combined depth map is generated, stacking pairwise depth maps computed for each camera that are subsequently used to generate partial dense point clouds. These clouds are then used to compute the final dense cloud. During this process, additional well-suited noise filter algorithms are applied step-by-step to the overlapping regions [39].

At this stage of the processing, planes are routinely fitted to groups of neighboring pixels of the combined depth maps in order to compute the normal of the partial dense clouds; finally, clouds can be texturized using the colors extracted from the images.

The processing is followed by the meshing operation that consists essentially of a 3D surface reconstruction process for quickly transforming the dense point cloud into a triangulated surface. Moreover, the necessary triangulated model optimization and simplification is performed by means of the application algorithms well-implemented in the AgisoftMetashape[®] software package [63].

An option to build the texture clouds is available in the recent versions of this package, by which the natural color contents of the photographic images can be used to texturize the 3D final models using an RGB color scale.

The three colorized, high density, registered point clouds computed using the procedure described above and representing in detail the rock samples under study were format converted into the e57 format (namely, the file format for 3D laser scanner data exchange) and then processed with the JRC 3D Reconstructor[®] Vs 4.1.2 (Gexcel, Brescia, Italy) and the CloudCompare Vs 2.12.4 free software. Clouds were also manually edited and then filtered to remove noisy data; the resulting unified clouds were then converted into mesh models texturized with both natural colors and light intensity to be useful as input for professional engineering-style software such as CAD[®] [16,49].

2.5. Three-Dimensional Ultrasonic Tomography

Based on the 3D models obtained with the above described geomatic technique (CRP-SfM), 3D ultrasonic tomography (3D UT) was planned on significative samples of each investigated lithotype (Pietra Cantone, Tramezzario and Pietra Forte).

The 3D UT adequately describes the effects of rock properties on the ultrasonic signal propagation and highlights the presence of potential defects such as cracks, fissures and cavities inside the materials. The morphology of the shallow materials in each sample was determined from the 3D high-resolution digital photogrammetric models in order to design an optimal ultrasonic survey and provide a very good spatial coverage of the investigated samples.

The carbonate samples were prepared in a prismatic shape with an average size of 20 cm × 10 cm × 10 cm. Ultrasonic measurements were carried out by the transmission method according to the ISRM 2007, 2014 [64,65] using a portable Ultrasonic

Non-Destructive Digital Indicating Tester (PUNDIT Lab plus) device (Proceq, Schwerzenbach, Switzerland) that measures the time of propagation of ultrasonic pulses within the 0.1–9999.9 μs range with a precision of 0.1 μs . The PUNDIT Lab plus was interfaced with the portable oscilloscope Fluke 96B for the acquisition of the digital signals emitted and received from two transducers at a resonance frequency of 82 kHz. The silicone snug sheets were used as the best coupling agent [66] to guarantee the best contact between the transducers and materials. The transducers were placed on all faces of each sample with 25 mm of vertical spacing along parallel vertical profiles to surround the entire sample. Each station (on average 72 stations per sample) was alternately used as a transmitter and receiver. The transit time of the longitudinal ultrasonic waves between stations (source–receiver path) was measured along a very large number of paths (approximately 2400) and averaged over eight determinations. The mean of the measurements was computed not considering values with a deviation higher than 3%. In this study, only the first arrivals for each source–receiver path were considered and confidently associated to the longitudinal wave (P-wave). The use of the ultrasonic longitudinal signal (P-wave) in velocity detection is recommended in practical applications, since the first arrival of the ultrasonic signal can be recognized unambiguously as a P-wave arrival. Generally, the quality of first-arrivals is related to many experimental conditions and especially to the signal-to-noise (S/N) ratio. In a few cases in which a low S/N ratio was found, a filtering operation was applied to improve it. We preferred to hand-pick the first arrivals of the longitudinal waves for the tomographic analysis. In fact, the accurate determination of the first-arrival times is needed to guarantee the high quality of the tomographic solutions. In many experimental conditions, the automated picking of first-arrivals can be a very difficult task especially in the case of a low S/N ratio.

The propagation velocity of the P-wave is detected from the ratio of the length of the ray-path (source–receiver distance) to the transit time of the longitudinal ultrasonic signal.

The 3D UT aimed to obtain a detailed elastic characterization of the carbonate samples consisted of the 3D reconstruction of the longitudinal velocity distribution inside the samples based on the P-wave travel times between the different source–receiver pairs precisely located on the base of the 3D high-resolution digital photogrammetric models. With many intersecting ray paths between different source and receiver positions around the sample, it is possible to reconstruct a detailed 3D field velocity of the elastic waves. In this study a tomographic inversion was applied to the ultrasonic data (measured travel times) to produce the 3D velocity model. This was determined starting from the P-wave first-arrival times as input data for the simultaneous iterative reconstruction technique (SIRT) [67,68], considering curved ray tracing to account for the heterogeneous velocity structure. The iterative reconstruction technique involves successive approximations to correct for an arbitrary initial velocity model. In order to obtain a realistic and not an arbitrary starting velocity model as input for the SIRT to invert travel-time data, a methodology based on the cross-correlation function (CCF) was used [69]. Starting from the initial velocity model, the SIRT algorithm is followed by computing the travel times for each source/receiver path. After this, the calculated and picked times are compared and a correction factor for the time discrepancy is applied to the velocity value of every cell (voxel) affecting the model. In this way, the initial velocity model is modified by repeated cycles, and the iterative process goes on until the necessary accuracy is achieved. In this study the entire processing sequence was repeated for 20 iterations which allowed it to obtain the final velocity model. This number of iterations was found appropriate to achieve the best representation of the 3D distribution of the longitudinal velocity within the investigated volumes and can be considered a good compromise between the resolving power and the reliability of the final velocity model.

The 3D rendering of the resulting velocity distribution inside the samples as a result of the tomographic inversion procedure was carried out using the Voxler v. 4.3.771 by Golden Software, which allows us to manipulate and organize large quantities of data in a convenient and effective manner. The 3D representation of the field velocity and the possi-

bility to visualize it through the 3D data volume facilitate the analysis and interpretation of the results. The 3D volume visualization with zooming and rotation allows a better understanding of the relationship between velocity variations and material properties for analysis and accurate interpretation. Furthermore, it is possible to create in an interactive manner as many slices as necessary, vertical or horizontal, that also help the interpretation. By observing the development of the velocity variations from slice to slice, the interpreter can acquire a good feel of their spatial development in the investigated volume.

3. Results and Discussion

3.1. Thin Section Analysis

The textural characteristics of the studied lithotypes were analyzed by optical microscopy, with reference to the presence of matrix or cement, as well as content, type and arrangement of the allochems. OM observations were integrated and enhanced by SEM in order to define the bioclast packing and the different grains–matrix or grains–cement relationships, while pointing out the different types of primary and secondary pores. The porosity detected by OM can be classified as mesoporosity [70], while the pores analyzed by SEM can be classified as microporosity [70].

Pietra Cantone is a bioclastic limestone with a mud-supported or micritic texture, mainly characterized by the remnants of foraminifera (Figure 2a) and other bioclasts ranging from 100 μm to 2.5 mm. The matrix is a carbonate mud made up of microcrystals of micrite. Within the micrite cement, the presence of iron oxides and terrigenous components such as quartz, feldspar and biotite is common (Figure 2b). The presence of iron oxides gives this lithotype its typical yellow color. According to the carbonate rocks classification of Dunham (1962) [71], the Pietra Cantone can be classified as mudstone–wackestone. The mesoporosity values of Pietra Cantone observed with OM has values from 7% to 25%. The mesoporosity is characterized by primary interparticle pores that can evolve into forms of secondary porosity, such as vug porosity, due to dissolution processes (Figure 2c,d). The SEM observations showed that Pietra Cantone is characterized mainly by a micropore network of well-connected interparticle pores with a mean size of 2 μm (Figure 2e,f), concentrated in the micrite [18]. This primary microporosity in the mud matrix is the main cause that makes this rock hygroscopic and highly susceptible to degradation.

Tramezzario is a grain-supported limestone rich in bioclasts with sizes ranging from 500 μm to 4 mm. The bioclasts are mostly made from well-sorted, sub-rounded algal fragments (Figure 3a) and bioclasts of other organism such as mollusks, bryozoa and crustacea, supported by a sparry calcite cement (Figure 3b). Tramezzario, according to the Dunham classification (1962) [71], can be defined as grainstone–packstone. In Tramezzario, the porosity is 10% on average, but it can reach 20% in deep sea facies, richer in carbonate mud. The mesoporosity observed at OM is a secondary porosity mainly of the channel, moldic, intraparticle and fracture types (Figure 3c,d). Except for the fracture type, these pores occur due to dissolution processes and are well connected. With SEM, the Tramezzario is characterized by single subhedral–anhedral calcite microcrystals (sizes 2–3 μm) or by polyhedral aggregates of calcite. Intercrystal pores [72] with sizes between 4 μm and 5 μm (Figure 3e) represent the main microporosity of the Tramezzario. These pores, located within the sparry calcite cement are generally interconnected, representing the preferential path on which the phenomena of dissolution act. The dissolution, therefore, determines the development of secondary pores such as vugs (Figure 3f) and channels.

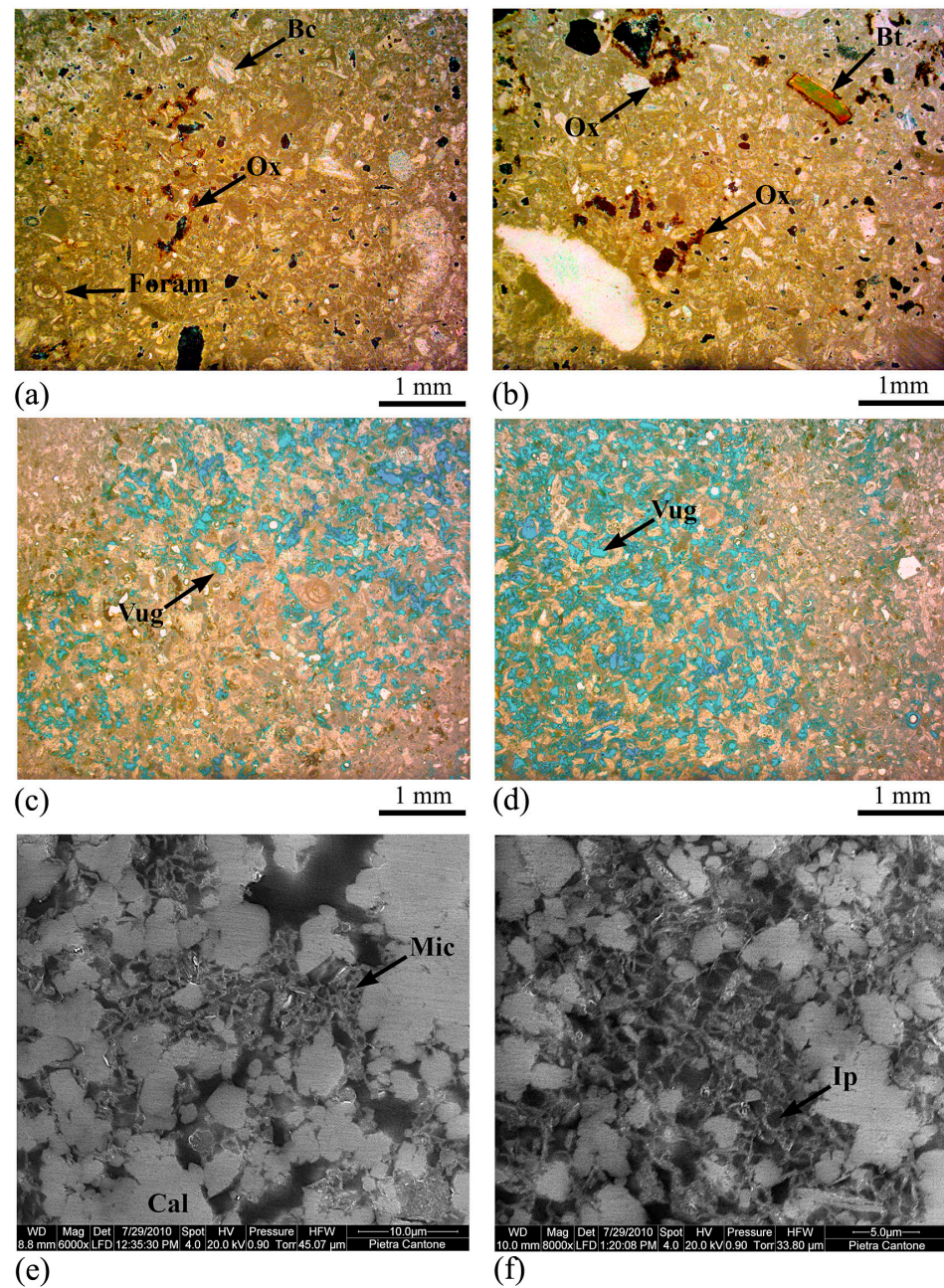


Figure 2. Textural characteristics of Pietra Cantone: (a) Mud-supported texture with bioclasts (Bc), foraminifera (Foram) and iron oxide (Ox); OM cross polarized light. (b) Iron oxide (Ox) and biotite (Bt) crystal; OM cross polarized light. (c) Vug secondary porosity (Vug); OM plane polarized light. (d) Vug secondary porosity (Vug) in a particularly porous sector of the rock; OM plane polarized light. (e) Micrite (Mic) microcrystals and calcite (Cal); SEM image. (f) Interparticle microporosity (Ip) in the microcrystalline carbonate mud; SEM image.

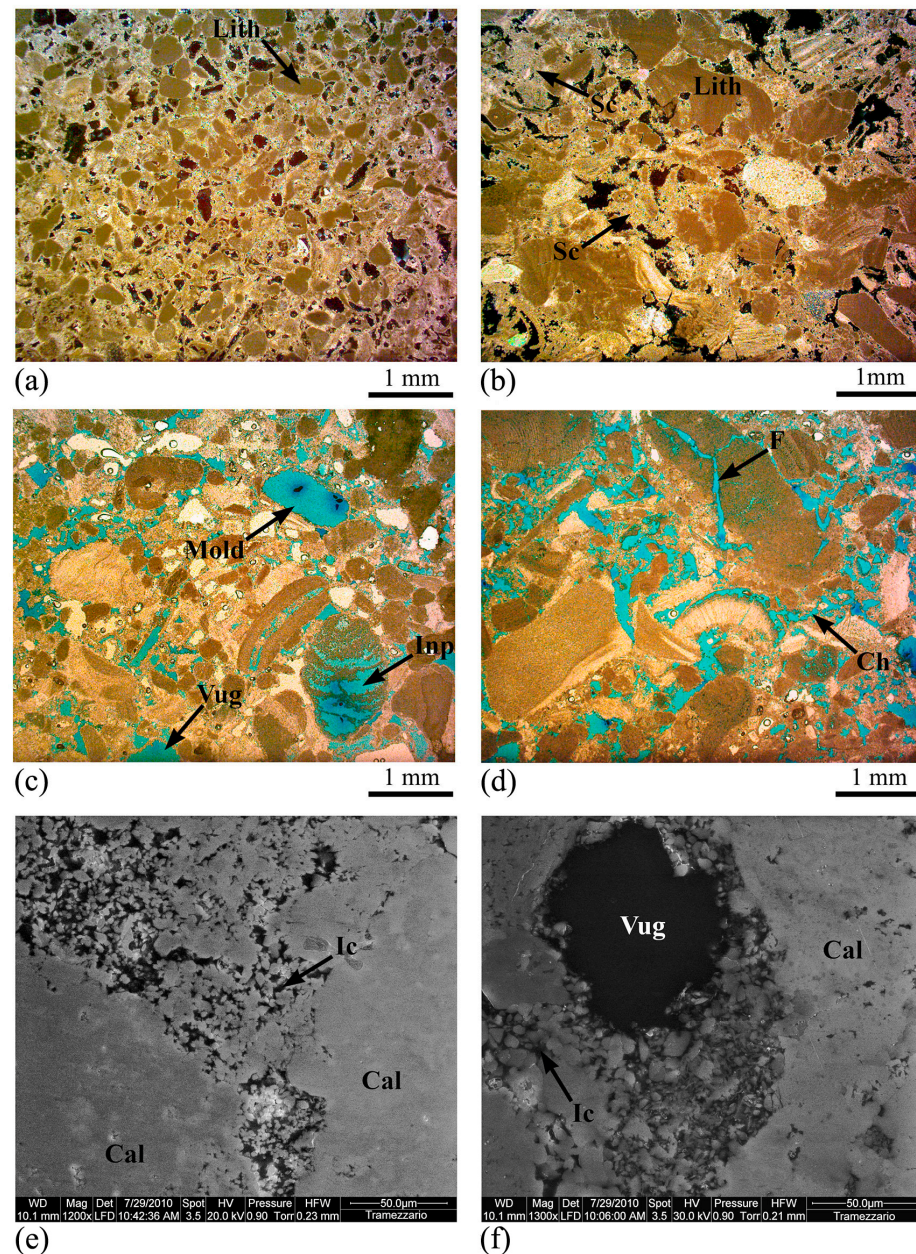


Figure 3. Textural characteristics of Tramezzario: (a) Grain-supported texture with bioclasts of Lithothamnium algae (Lith); OM cross polarized light. (b) Sparry calcite (Sc) among the bioclasts of Lithothamnium algae (Lith); OM cross polarized light. (c) Vug, moldic (Mold) and intraparticle (Inp) secondary porosity; OM plane polarized light. (d) Channel (Ch) and fracture (F) secondary porosity; OM plane polarized light. (e) Intercrystal (Ic) pores among the calcite (Cal) crystals; SEM image. (f) Vug and intercrystal (Ic) porosities and calcite (Cal); SEM image.

Pietra Forte has the characteristics of biohermal–biostroma limestones. This is a rock-preserved biogenic texture, whose original components, mainly Lithothamnium algae (Figure 4a,b), were bound and encrusted together during deposition and stayed substantially in the position of growth. According to the Dunham classification [71], the Pietra Forte is a boundstone, mainly made up of Lithothamnium algae, which embody bioclasts of other organisms such as bivalves, bryozoans, etc., all cemented by sparry calcite, which makes the rock very compact and scarcely porous at the microscopic level. The porosity of Pietra Forte is about 1%–4%, mainly of the secondary type, due to post diagenetic dissolution phenomena. The observed pores are of intraparticle, vug, channel

and fracture types (Figure 4c,d). However, pores of the primary type, such as the growth framework due to the growth structures of Lithothamnium algae, have been observed in a few cases. The majority of these pores are now filled with sparry calcite (Figure 4c).

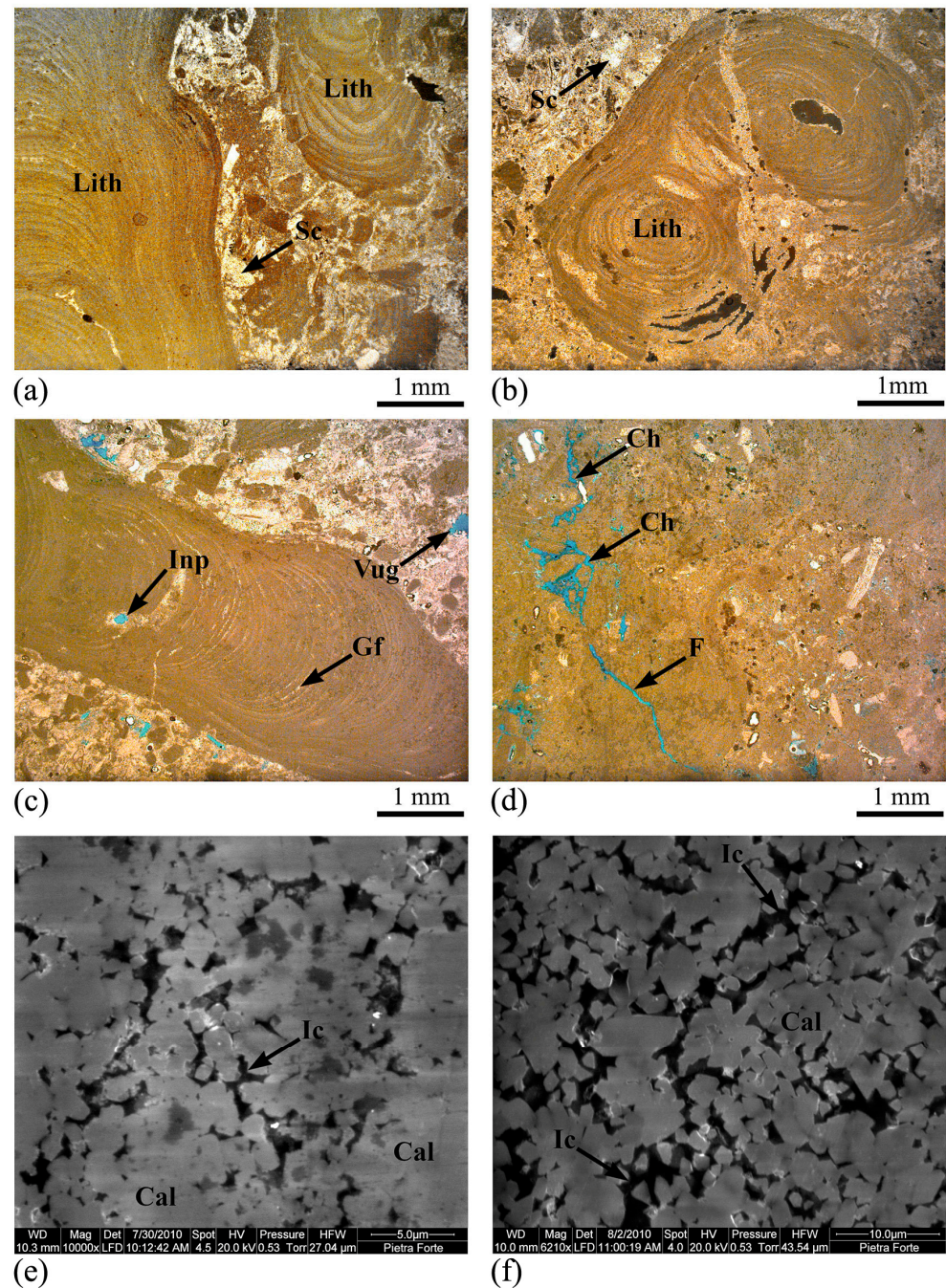


Figure 4. Textural characteristics of Pietra Forte: (a) Biogenic texture rich in Lithothamnium algae (Lith) well-cemented by sparry calcite (Sc); OM cross polarized light. (b) Another fossil of Lithothamnium algae (Lith) with sparry calcite (Sc); OM cross polarized light. (c) Vug and intraparticle (Inp) secondary porosity. The primary porosity due to the growth structure of algae, called the growth framework (Gf), filled by the sparry calcite; OM plane polarized light. (d) Channel (Ch) and fracture (F) secondary porosity; OM plane polarized light. (e) Intercrystal (Ic) pores among the calcite (Cal) crystals; SEM image. (f) Intercrystal (Ic) porosity in a more porous sector of the rock and calcite (Cal); SEM image.

Pietra Forte is exclusively made up of calcite [57], characterized by single subhedral microcrystals (sizes 2–3 μm) or polyhedral aggregates of calcite. With SEM, Pietra Forte is characterized by an intercrystal microporosity [72] with dimensions of pores smaller than 4 μm (Figure 4e,f). This scarce microporosity is due to the presence of carbonate cement, which during lithogenesis filled the spaces between the algal structures and the other bioclasts, making this lithotype very compact. However, when the pores are communicating, they allow the infiltration of water rich in CO_2 that causes dissolution and enlargement of the pores up to the formation of karst cavities.

3.2. MIP Analyses

The results of the MIP study are summarized in Figure 5a–c, where three representative curves showing the typical patterns of the pore-throat size (diameter) distribution of Pietra Cantone, Tramezzario and Pietra Forte are reported. In Figure 5a we can observe that in Pietra Cantone, the sizes of pore-throats are prevalently in the 0.2–7 μm range. In the MIP curve of Tramezzario (Figure 5b), the sizes of pore-throats range mainly from 1 μm to 90 μm . The Pietra Forte representative MIP curve shows pore-throat diameters in the range from about 0.04 μm to 0.4 μm (Figure 5c).

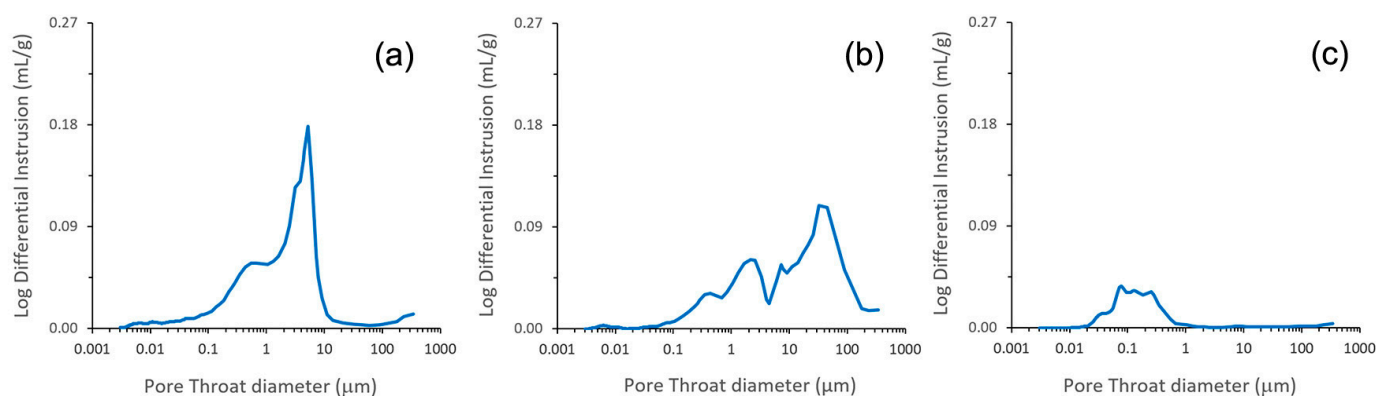


Figure 5. MIP curves highlighting the pore-throat size distributions of three representative samples of the Calcari di Cagliari: (a) Pietra Cantone; (b) Tramezzario; (c) Pietra Forte.

In Table 1, some of the most important MIP parameters of the pore structures of the studied carbonate rocks are reported.

Table 1. MIP parameters of Calcari di Cagliari.

Calcari di Cagliari	Sample	d_{50} (μm)	Bulk Density (g/cm^3)	Skeletal Density (g/cm^3)	Porosity (%)	Permeability (mD)	Tortuosity
Pietra Cantone	PC1	1.69	2.07	2.77	25.35	8.16	21.23
	PC2	8.85	1.62	2.65	38.71	215.10	5.34
	PC3	1.03	1.89	2.66	28.86	0.37	16.01
	PC4	1.78	1.89	2.72	30.41	9.16	20.20
	PC5	2.45	1.91	2.68	28.72	10.93	23.25
Tramezzario	TR1	12.06	1.58	2.67	40.85	557.92	3.01
	TR2	3.06	2.33	2.69	13.40	26.02	3.73
	TR3	10.67	1.99	2.71	26.61	506.42	4.45
	TR4	17.58	2.09	2.73	23.25	702.28	3.90
	TR5	14.70	1.89	2.75	31.00	1168.12	3.68
Pietra Forte	PF1	0.13	2.53	2.70	6.26	0.11	2.39
	PF2	0.20	2.46	2.71	9.24	0.12	6.55
	PF3	0.15	2.46	2.70	8.74	0.11	6.21
	PF4	16.13	2.51	2.69	6.66	1044.22	2.36
	PF5	0.05	2.65	2.71	2.21	0.16	2.03

d_{50} = median pore-throat diameter.

In the Pietra Cantone samples, the median pore-throat diameters (d_{50}), corresponding to 50% of mercury saturation, range from 1.03 μm to 8.85 μm . They prevail in the range of microporosity (Table 1) according to its textural features (Figure 2a,b). Bulk density values are from 1.62 g/cm^3 to 2.07 g/cm^3 and the values of skeletal density are between 2.65 g/cm^3 and 2.77 g/cm^3 . All samples of Pietra Cantone show high values of effective porosity ranging from 25.35% to 38.71%. The values of permeability from 0.37 mD to 10.93 mD in four samples (PC1, PC3, PC4 and PC5) are low (Table 1). On the other hand, except for the PC2 sample (Table 1), the generally high tortuosity values (between 16.01 and 23.25) of these samples are compatible with the intrinsic nature of this lithotype and texture, that is prevalently made up of small-sized particles (micrite matrix) as deduced by OM and SEM. The PC2 has a high permeability value of 215.10 mD (Table 1) that is compatible with its large size of pore-throats (d_{50} of 8.85 μm). In this sample, the MIP results highlight the highest value of effective porosity (at about 40%) related to meso- and macropores (Figure 2c–f) interconnected by larger throats which favor the passage of fluids into the rock. The low tortuosity value of 5.34 is compatible with its high permeability value.

In the Tramezzario samples, the median pore-throat diameters (d_{50}), from 3.06 μm to 17.58 μm (Table 1), are generally higher than the pore-throat sizes measured in Pietra Cantone and Pietra Forte. They prevail in the range of mesoporosity as also highlighted by OM observation (Figure 3c,d). Bulk density values range between 1.58 g/cm^3 and 2.33 g/cm^3 and skeletal density values are from 2.67 g/cm^3 to 2.75 g/cm^3 (Table 1). As for Pietra Cantone, the Tramezzario shows high values of effective porosity (in the 23.25%–40.85% range), except for TR2 sample (13.40%). Permeability values are in the 26.02–1168.12 mD range. The low values of tortuosity, from 3.01 to 4.45 (Table 1), favor the circulation of fluids into the pore network. The generally high permeability and low tortuosity are also related to the interconnected porosity at the meso- and microscale as also observed by OM and SEM (Figure 3c,f).

Pietra Forte limestone shows median pore-throat diameters (d_{50}) from 0.05 μm to 0.13 μm (microporosity), except for the PF4 sample with a median throat diameter of 16.13 μm (Table 1). Bulk and skeletal densities range from 2.46 g/cm^3 to 2.65 g/cm^3 and from 2.69 g/cm^3 to 2.71 g/cm^3 , respectively. These samples show values of effective porosity from 2.21% to 9.24% and permeability from 0.11 to 0.16 mD, except for PF4 (1044.42 mD), due to its large pore-throat size. The tortuosity of Pietra Forte is quite low ranging from 2.03 to 6.55 and related to a pore network not articulated depending on the intrinsic textural features of this rock (Figure 4a–f). In general, Pietra Forte is less porous and better cemented than Pietra Cantone and Tramezzario [73] with low values of porosity and permeability. Nevertheless, in some cases (e.g., the PF4 sample), the presence of fractures and dissolution phenomena forming “karst” with caves and fissures can increase its permeability [73].

3.3. CRP

Using the integrated procedure described above, the three high-resolution 3D unstructured filtered and aggregated prismatic-shaped point clouds were computed. They were texturized with the natural colors represented in an RGB scale as detected from the 2D photo images with the aid of the AgisoftMetashape photogrammetric package (Figure 6). These point clouds were subsequently texturized also with the intensity of the light containing the reflectance of the materials making up the samples under study, which can be directly compared with the velocity patterns from the high-frequency ultrasonic methodology.

To account for the accuracy of the HR 3D models computed with the CRP methodology, we first estimated the geometrical anomalies of the point clouds of the Pietra Cantone, Tramezzario and Pietra Forte prismatic-shaped samples with the aid of the RANSAC shape detector utility of CloudCompare. Six planes fitted to the faces of each sample were automatically computed and then meshed. The residuals of the point cloud with respect to the planes using the corresponding meshes as references were computed with the “cloud to mesh” distance (C2M) function of the package. After aggregating the six

faces' geometrical anomalies with the merge function of CloudCompare, the statistical Gauss function was subsequently applied in order to estimate the standard deviation of the means of the geometrical anomaly aggregated clouds of the three samples [74]. The results of this last computation are represented in the three histograms of Figure 7.

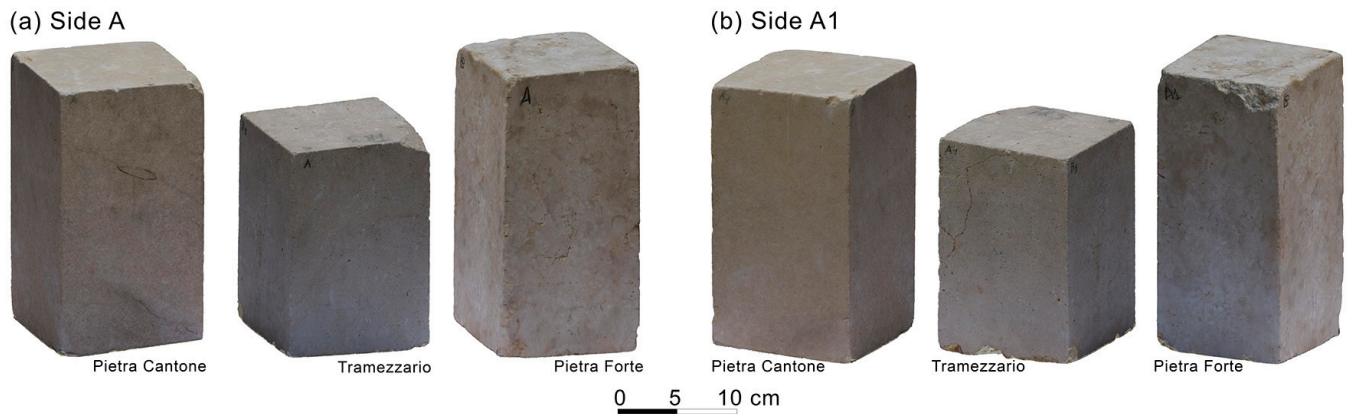


Figure 6. (a) Side A view of the HR 3D models of the three prismatic samples under study textured with natural colors. (b) Side A1 view.

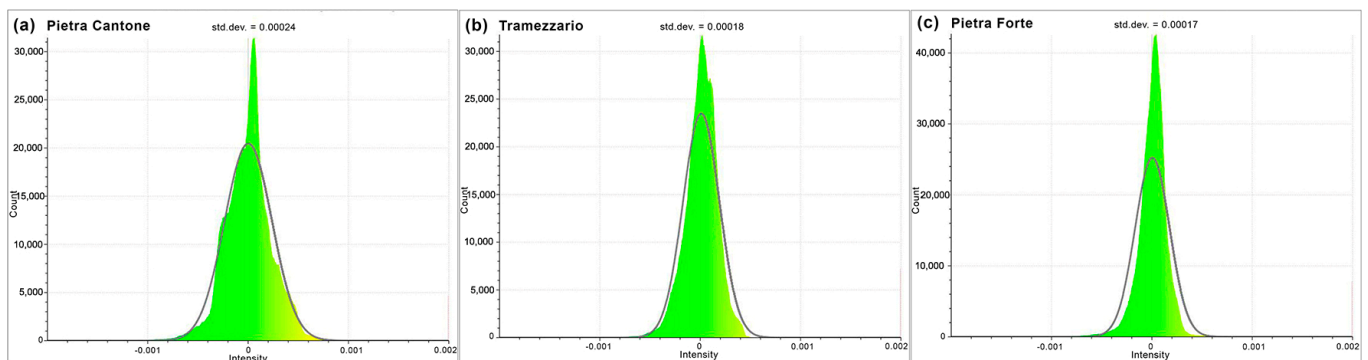


Figure 7. Statistical Gauss function applied to the geometrical anomalies of the three HR 3D models of the prismatic samples under study. The standard deviations of the three models are computed to account for the model accuracy.

As can be appreciated in the figure, the data appear to follow a Gaussian statistical distribution, and the standard deviations of the three 3D models are 0.24, 0.18 and 0.17 mm for the Pietra Cantone, Tramezzario and Pietra Forte sample clouds, respectively, testifying to the great accuracy of the CRP methodology. Finally, considering that for a 3D Gaussian distribution 99% of the confidence region is approximately reached by multiplying the standard deviations by a factor of three, the accuracy of the corresponding 3D models ranges from 0.7 mm for the Pietra Cantone lithotype to 0.5 mm for the Pietra Forte and Tramezzario lithotypes. The greater the accuracy of the model, the smaller the standard deviation. This comparison testifies that according to CRP results, the most compact material of the Calcari di Cagliari formation is Pietra Forte followed by Tramezzario, while Pietra Cantone actually appears to be the least compact.

3.4. Ultrasonic Tomography

The interpretation of the integrated geomatic and geophysical data proposed in this study has been supplemented by petrographical and petrophysical data. The textural and compositional characteristics of the carbonate rocks, as well as the quantity and size of the pores, and the dominant pore types exert a profound influence on the geophysical responses [49,51,75,76]. Therefore, in order to emphasize the benefit that derives from applying the proposed non-destructive multi-technique approach in the characterization

of stone materials, it is fundamental to understand the link between petrographical and geophysical properties. Moreover, by understanding the link between petrographic and geophysical parameters, certain ambiguities in geophysical interpretation can be avoided in many practical cases. The composition, texture and type of porosity predispose a stone material to different types and intensities of degradation, which can be recognized and qualified both superficially and in depth by using the geomatic and geophysical methods presented here.

The results of the 3D UT showing high-resolution images of the P-wave velocity distribution on the three significant samples of the Calcari di Cagliari formation are presented together with the 3D CRP high-resolution models and significant thin section images in Figures 8–13. As tomographic results in the above figures, the horizontal tomographic slices extracted from the 3D UT data volume are also reported. The location and orientation of the slices were decided interactively for a detailed mapping of the internal distribution of the elastic characteristics of the investigated samples. As a first result of the ultrasonic evaluation, the velocity ranges were detected for each sample. The velocities range from 2320 m/s to 4390 m/s in Pietra Cantone, from 2750 m/s to 5480 m/s in Tramezzario and from 3500 m/s to 7500 m/s in Pietra Forte. The differences in the longitudinal velocity of the three lithotypes are justified by the complex physical and petrographical properties that characterize the carbonate rocks due to their complex pore system and textural heterogeneities as seen in the results from OM, SEM and MIP.

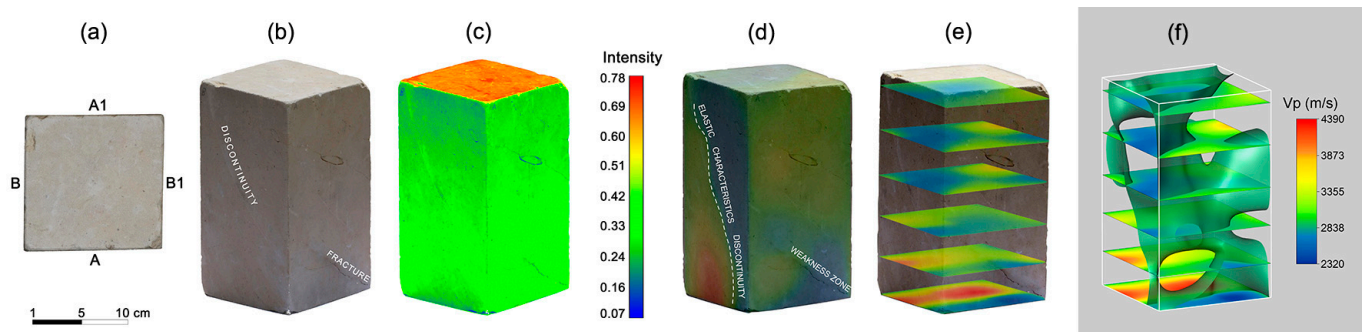


Figure 8. Results of the 3D analyses by the integrated approach for the Pietra Cantone sample. (a) Localization of the different faces of the sample. (b) 3D HR CRP model texturized with natural colors and represented with an RGB scale. (c) 3D HR CRP model texturized with the intensity of ambient light. (d) 3D ultrasonic tomography incorporated within the 3D HR CRP model. (e) Tomography horizontal slices. (f) Isosurface of 2800 m/s with horizontal slices.

As a general remark, it can be observed that the shallow features (e.g., presence of fractures of different origins, discontinuities and chromatic anomalies) of the examined samples as observed in the CRP models (Figures 8b,c, 10b,c and 12b,c) match the longitudinal velocity distribution in the shallow part of the materials (Figures 8d, 10d and 12d), and in many cases they also influence the elastic conditions of their inner parts.

In the Pietra Cantone sample, the mechanical discontinuity and fracture that affect its shallow part, which are highlighted well by the CRP models (Figure 8b,c), determine a significant decrease in the longitudinal velocity (blue zones in Figure 8d,e). Furthermore, the results of the 3D UT indicate that the above mechanical discontinuity evolves into the inner part of the sample as a discontinuity of elastic characteristics along the longitudinal development of the sample. The fracture observable in the CRP model (Figure 8b) does not develop in depth as the low velocity zone is limited to the shallowest parts, as can be observed in Figure 8e. The isosurface of 2800 m/s shown in Figure 8f represents the boundary between high (red) and low (blue) velocity zones. Considering the OM, SEM and MIP results, it can be deduced that discontinuity, fractures and other defects mainly occur in sectors where the rock is most vulnerable on account of a high concentration of secondary porosity of the vug type, which depletes the elastic properties of the carbonate material

(low velocity zones) (Figure 9a,b). The vug porosity is probably due to the dissolution processes caused by a permanent presence of water in sectors rich in carbonate mud. As observed by SEM, the mud is characterized by a high percentage of primary micropores of the interparticle type which, when combined, form a porous network that negatively affects the velocity of the ultrasonic pulses, and therefore the elastic characteristics of the rock. However, in the analyzed sample, higher velocity values (approximately 3800–4300 m/s) were also detected. They are related to more compact rock sectors, where the percentage of pores, especially of the secondary type, is low (Figure 9a,c). This condition, due to a better compaction in the diagenetic phase and almost absent dissolution phenomena, enhances the elastic properties of the rock and favors the propagation of the longitudinal ultrasonic pulses.

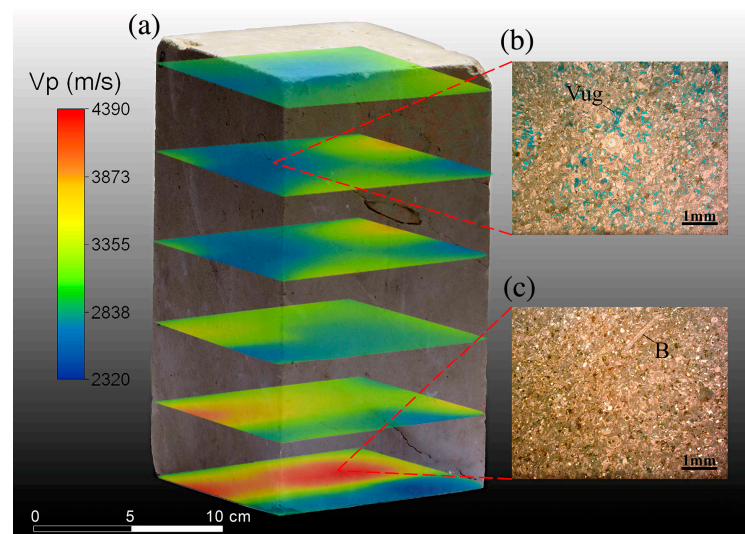


Figure 9. Pietra Cantone sample: integrated analysis of ultrasonic tomography and thin sections. (a) Tomography horizontal slices incorporated within the 3D HR CRP model. (b) Microscopic features of a porous sector of the sample; OM plane polarized light; thin section treated with blue dye epoxy resin. Vug (vug secondary porosity). (c) Microscopic features of a compact sector of the sample; OM cross polarized light. B (bioclast).

In the sample of Tramezzario, the fracture, which is well visible on the CRP models (Figure 10b,c), mainly influences the elastic conditions of the shallow material since it does not develop significantly in depth, as can be deduced from the limited extension of the low velocity zones (blue zones in Figure 10d,e) detected by 3D UT. The isosurface of the 3800 m/s shown in Figure 10f represents the passage between high (red) and low (blue) velocity zones. In the Tramezzario sample, the best cemented sectors, where the deposition of carbonate cement prevailed with respect to the dissolution processes, are characterized by higher velocity values (4700–5480 m/s) typical of a compact carbonate rock with good elastic characteristics (Figure 11a,b).

The lower velocity values (approximately 2750–3500 m/s) detected in a few sectors of the sample are attributable to a greater concentration of secondary pores of channel, vug and fracture types. These secondary pores involve diffraction phenomena causing scattering of the elastic waves, and consequently attenuation of the ultrasonic signal propagation (Figure 11a,c) [77].

In the Pietra Forte sample (Figure 12a–f), which is characterized by higher velocity values compared to previous lithotypes, the weak fracture highlighted by the 3D CRP models does not produce significant variations in the elastic behavior of the rock. This is a consequence of the fact that this fracture is partly cemented and limited to the shallow parts of the material, as can be deduced from the 3D UT results (Figure 12d,e). The isosurface of the 5200 m/s shown in Figure 12f represents the passage between high (red) and low

(blue) velocity zones. It can be noted that in some sectors of the analyzed sample, the ultrasonic signals propagate with lower velocity values (3500–4000 m/s). In these sectors, different types of secondary porosity such as channel, fracture and karst microcavities negatively affect the elastic behavior of the rock (Figure 13a,b). The elastic characteristics of this rock are excellent in sectors characterized by high velocity values (6000–7500 m/s). In these sectors, Pietra Forte is almost free of pores and very well cemented by spathic calcite (Figure 13a,c).

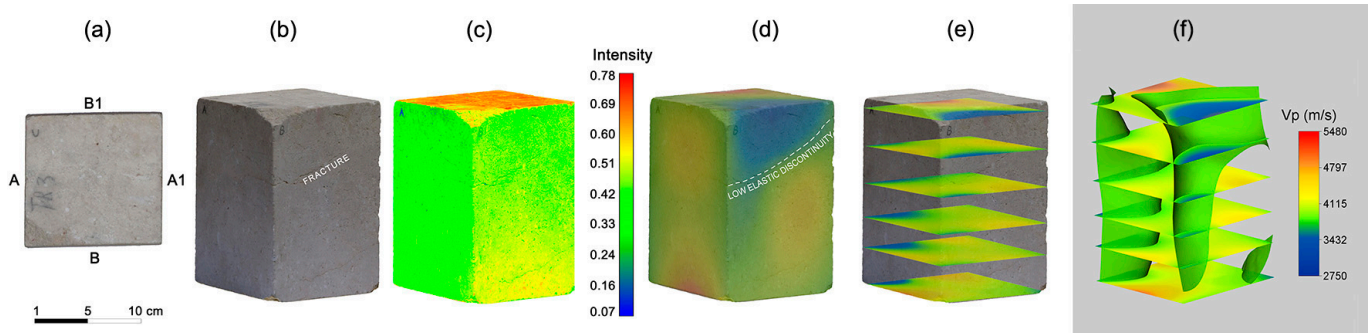


Figure 10. Results of the 3D analyses by the integrated approach for the Tramezzario sample. (a) Localization of the different faces of the sample; (b) 3D HR CRP model textured with natural colors and represented in a RGB scale; (c) 3D HR CRP model textured with the intensity of ambient light; (d) 3D ultrasonic tomography incorporated within the 3D HR CRP model; (e) Tomography horizontal slices; (f) Isosurface of 3800 m/s with the horizontal slices.

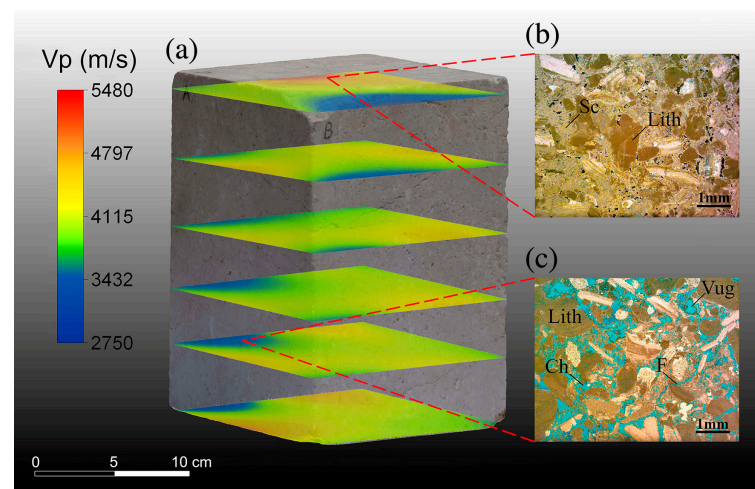


Figure 11. Tramezzario sample: integrated analysis of ultrasonic tomography and thin sections. (a) Tomography horizontal slices incorporated within the 3D HR CRP model. (b) Microscopic features of a compact sector of the sample; OM cross polarized light. Sc (sparry calcite); Lith (Lithothamnium algae). (c) Microscopic features of a porous sector of the sample; OM plane polarized light; thin section treated with blue dye epoxy resin. Vug (vug secondary porosity); Lith (Lithothamnium algae); Ch (channel porosity); F (fracture).

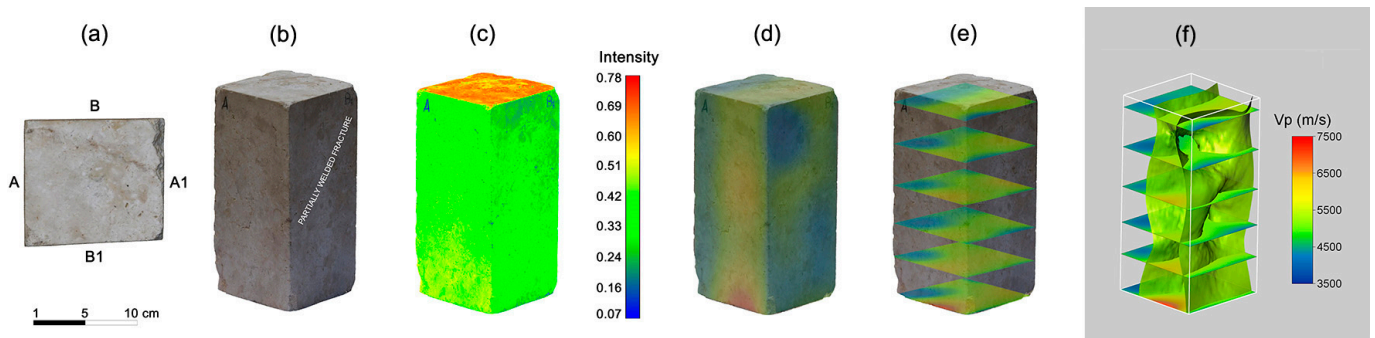


Figure 12. Results of the 3D analyses by the integrated approach for the Pietra Forte sample. (a) Localization of the different faces of the sample. (b) 3D HR CRP model texturized with natural colors and represented with an RGB scale. (c) 3D HR CRP model texturized with the intensity of ambient light. (d) 3D ultrasonic tomography incorporated within the 3D HR CRP model. (e) Tomography horizontal slices. (f) Isosurface of 5200 m/s with horizontal slices.

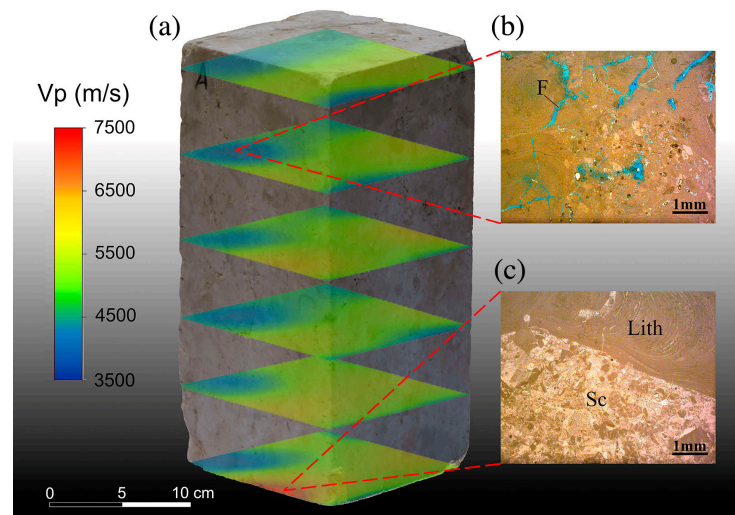


Figure 13. Pietra Forte sample: integrated analysis of ultrasonic tomography and thin sections. (a) Tomography horizontal slices incorporated within the 3D HR CRP model. (b) Microscopic features of a porous sector of the sample; OM plane polarized light; thin section treated with blue dye epoxy resin. F (fracture secondary porosity). (c) Microscopic features of a compact sector of the sample; OM cross polarized light. Lith (Lithothamnium algae); Sc (sparry calcite).

4. Concluding Remarks

The integrated non-invasive approach for the characterization of the carbonate rock samples of the Calcarei di Cagliari formation carried out in this study by different techniques can effectively highlight the characteristics of the stone materials and reduce uncertainties that may arise using a single methodology. The integration of different datasets demonstrates that it is capable of solving ambiguities by linking different types of information.

With the aid of close-range photogrammetry (CRP) based on the structure from motion (SfM) methodology, high-resolution 3D models of the studied samples with an accuracy of better than 1mm were computed. For every prismatic sample, a cloud of about 10 million points was computed and texturized, both with the natural colors derived from the 2D digital images and the intensity of the backscattered natural light. The accuracy of the models ranges from about 0.7 to 0.5 mm and was determined starting from the geometrical anomalies computed as residuals with respect to the six planes fitting to the prismatic-shaped sample faces. As a matter of fact, the greater the accuracy the lower the noise due to the presence of defects like voids, cracks and discontinuities of the rock. In fact, the

accuracy of the models of the studied samples is greater for Pietra Forte (RMSE = 0.51 mm), while the Tramezzario is characterized by a comparable noise (RMSE = 0.54 mm). The least consistent material appears to be Pietra Cantone that is characterized by an accuracy closer to 1mm (RMSE = 0.72 mm).

Therefore, the CRP methodology is very useful for the analysis of the shallow part of stone materials and provides useful data suitable to different applied research branches. Furthermore, the large amount of acquired metric information was useful for an accurate planning of 3D ultrasonic tomography and for the locations of the ultrasonic sources and receiver stations. The 3D high-resolution CRP models allowed us to reconstruct the ultrasonic survey geometry precisely for an accurate processing of the 3D tomographic data and effective restitution of the tomography results. In fact, the 3D ultrasonic volumes were incorporated within the 3D high-resolution CRP models. This integration became a tool for efficiently understanding the possible links between the conditions of the shallow and inner parts of the sample.

The 3D ultrasonic tomography was effective in efficiently reconstructing a detailed image of the longitudinal velocity distribution inside the samples. This technique, complemented with geomatic and petrographic–petrophysical data, represents a powerful high-resolution method for investigating the inner elastic condition of the stone materials, while identifying heterogeneities, precise locations and sizes of defects or damaged zones at a different scales. From the integrated analysis of the geomatic–geophysical data with the petrographic–petrophysical data, it can be seen that factors such as mineralogical composition, structure and geometry of the pores, type of pores, tortuosity and cementing material need to be taken into consideration while interpreting the geomatic and geophysical responses of the carbonate rocks. Understanding the dependence of the longitudinal velocity on the above rock properties may be important for many practical applications, such as the diagnostic process of the conservation state of monumental structures, rock mass qualification for engineering purposes, quarrying activities, mining and others.

From the integrated analysis carried out in the present study, it appears that the carbonate lithotypes of the Calcari di Cagliari are considerably heterogeneous and characterized by different elasto-mechanical conditions, as demonstrated by the velocity ranges that characterize them. According to their different elastic behaviors, considering the geomatic responses and their petrographical and petrophysical characteristics, it is possible to associate each lithotype with a different susceptibility to degradation.

Pietra Forte is less porous and better cemented than Tramezzario and especially Pietra Cantone. Therefore, Pietra Forte is the highest quality carbonate rock investigated in this study because of its textural and petrophysical properties that enhance its elastic behavior. Among the carbonate lithotypes under study, Pietra Forte appears to be the most mechanically resistant even when used as a construction material, and it ensures better performance than the other carbonate rocks under study. Therefore, this lithotype is in general less susceptible to degradation, except for some situations in which there is a prevalence of a secondary porosity of the vug type as a result of the dissolution process of calcite. In these conditions, the dissolution process can lead to an increase in the size and interconnection of the pores, which can favor its degradation at the microscale giving rise to a karst system at the macroscale.

At the sample scale, the Tramezzario lithotype is unaltered and quite compact as deduced from the geomatic and geophysical responses. Tramezzario is a grain-supported limestone rich in bioclasts cemented by sparry calcite. This characteristic increases its elastic behavior and thus its longitudinal velocity. In the Tramezzario lithotype, generally characterized by well-interconnected macroporosity and microporosity, the process of degradation mainly depends on the easy passage of the fluids (high permeability and low tortuosity) into the well-interconnected pore network. Therefore, in this rock, degradation processes do not occur homogeneously and are generally focused into localized zones depending on the local condition of the pore network.

The most vulnerable lithotype, and therefore most subject to degradation, appears to be the Pietra Cantone lithotype. In this rock, in fact, there were high concentrations of secondary porosity of the vug type, probably caused by the occurrence of dissolution process. Moreover, the diffuse interparticle microporosity concentrated in the fine micrite matrix tends to capture the fluids (e.g., moisture) and retain them in the pore network. Consequently, Pietra Cantone is characterized by high hygroscopicity that favors its subsequent chemical weathering and physical disintegration, as observed when used as a building material. These characteristics worsen the elasto-mechanical behavior of the rock and favor the presence of different types of discontinuities and weakness zones. Therefore, in a framework of a monument protection project, the Pietra Cantone represents the construction material whose conditions need to be constantly monitored over time.

The presented integrated approach aimed at characterize the carbonate rocks of the Calcari di Cagliari formation and evaluate their susceptibility to degradation, can also be useful to determine the effectiveness of restoration actions and to check the compatibility between original and restoration materials.

The results presented in this paper demonstrate that the proposed integrated use of non-invasive complementary methods, such as CRP and 3D ultrasonic tomography complemented, where possible, with petrographic information, would guarantee the reproducibility of the measurements both at the laboratory and field scales, giving valuable information about potential changes in time in the rock condition. The integrated use of CRP and ultrasonic tomography can be considered a preventive and non-invasive conservation tool in line with current trends in the protection of cultural heritage, which require iterative and flexible procedures as opposed to interventional conservation actions, that are generally invasive and more expensive.

Author Contributions: S.F. and G.C. conceived the integrated non-invasive approach; F.C. performed the OM and SEM observations of the materials; G.C. and M.G.B. carried out the CRP survey and processed and interpreted the data; S.F. and F.C. planned and carried out the ultrasonic data acquisition; S.F. processed and interpreted the ultrasonic data and performed the integrated ultrasonic and petrographic–petrophysical data analysis with F.C. and P.L.; P.L. analyzed and interpreted the MIP data. All authors discussed the results and performed the integrated interpretation of the different datasets. All authors contributed to the drafting and revision of the manuscript. All authors have read and agreed to the published version of the manuscript.

Funding: This research was funded by Consorzio Interuniversitario per l’Ingegneria delle Georisorse (CINIGeo), Roma, Italy—research contract n. 376—2023. Resp. Sc.: S. Fais.

Data Availability Statement: Dataset available on request from the authors.

Conflicts of Interest: The authors declare no conflicts of interest.

References

1. Bianco, L. Geochemistry, Mineralogy and Textural Properties of the Lower Globigerina Limestone Used in the Built Heritage. *Minerals* **2021**, *11*, 740. [[CrossRef](#)]
2. Dionísio, A.; Martinho, E.; Grangeia, C.; Almeida, F. Examples of the Use of Non-Invasive Techniques for the Evaluation of Stone Decay in Portugal. *Key Eng. Mater.* **2013**, *548*, 239–246. [[CrossRef](#)]
3. Lisci, C.; Galhano, C.; Simão, J.; Pires, V.; Sitzia, F.; Mirão, J. Hydrophobic Coatings’ Efficiency and Limestones’ Resistance to Salt Crystallisation. *Sustainability* **2024**, *16*, 816. [[CrossRef](#)]
4. Proietti, N.; Calicchia, P.; Colao, F.; De Simone, S.; Di Tullio, V.; Luvidi, L.; Prestileo, F.; Romani, M.; Taù, A. Moisture Damage in Ancient Masonry: A Multidisciplinary Approach for In Situ Diagnostics. *Minerals* **2021**, *11*, 406. [[CrossRef](#)]
5. Roussel, E.; Vautier, F.; Voldoire, O.; André, M.-F.; Cassar, J.; Fronteau, G.; Phalip, B.; Thomachot-Schneider, C.; Toumazet, J.-P. Quantifying 450 Years of Limestone Weathering Induced by Salt Crystallization on Fortifications in Malta and Gozo. *Geomorphology* **2021**, *378*, 107614. [[CrossRef](#)]
6. Sitzia, F.; Lisci, C.; Mirão, J. Building Pathology and Environment: Weathering and Decay of Stone Construction Materials Subjected to a Csa Mediterranean Climate Laboratory Simulation. *Constr. Build. Mater.* **2021**, *300*, 124311. [[CrossRef](#)]
7. Aly, N.; Wangler, T.; Török, Á. The Effect of Stylolites on the Deterioration of Limestone: Possible Mechanisms of Damage Evolution. *Environ. Earth Sci.* **2018**, *77*, 565. [[CrossRef](#)]
8. Cantrell, D.L.; Hagerty, R.M. Microporosity in Arab Formation Carbonates, Saudi Arabia. *GeoArabia* **1999**, *4*, 129–154. [[CrossRef](#)]

9. Fais, S.; Casula, G.; Cuccuru, F.; Ligas, P.; Bianchi, M.G.; Plaisant, A.; Pettinau, A. A Contribution to the Geological Characterization of a Potential Caprock-Reservoir System in the Sulcis Coal Basin (South-Western Sardinia). *Energies* **2019**, *12*, 4524. [[CrossRef](#)]
10. Patzek, T.W.; Saad, A.M.; Hassan, A. Multimodal Carbonates: Distribution of Oil Saturation in the Microporous Regions of Arab Formations. *Energies* **2022**, *15*, 1243. [[CrossRef](#)]
11. Vázquez, M.A.; Galán, E.; Ortiz, P.; Ortiz, R. Digital Image Analysis and EDX SEM as Combined Techniques to Evaluate Salt Damp on Walls. *Constr. Build. Mater.* **2013**, *45*, 95–105. [[CrossRef](#)]
12. Christaras, B.; Auger, F.; Mosse, E. Determination of the Moduli of Elasticity of Rocks. Comparison of the Ultrasonic Velocity and Mechanical Resonance Frequency Methods with Direct Static Methods. *Mater. Struct.* **1994**, *27*, 222–228. [[CrossRef](#)]
13. Christaras, B. Non Destructive Methods for Investigation of Some Mechanical Properties of Natural Stones in the Protection of Monuments. *Bull. Int. Assoc. Eng. Geol.* **1996**, *54*, 59–63. [[CrossRef](#)]
14. Hrdina, M.; Surovy, P. Internal Tree Trunk Decay Detection Using Close-Range Remote Sensing Data and the PointNet Deep Learning Method. *Remote Sens.* **2023**, *15*, 5712. [[CrossRef](#)]
15. Puxeddu, M.; Cuccuru, F.; Fais, S.; Casula, G.; Bianchi, M.G. 3D Imaging of CRP and Ultrasonic Tomography to Detect Decay in a Living Adult Holm Oak (*Quercus ilex* L.) in Sardinia (Italy). *Appl. Sci.* **2021**, *11*, 1199. [[CrossRef](#)]
16. Bianchi, M.G.; Casula, G.; Cuccuru, F.; Fais, S.; Ligas, P.; Ferrara, C. Three-Dimensional Imaging from Laser Scanner, Photogrammetric and Acoustic Non-Destructive Techniques in the Characterization of Stone Building Materials. *Adv. Geosci.* **2018**, *45*, 57–62. [[CrossRef](#)]
17. Cara, S.; Valera, P.; Matzuzzi, C. Morphometric Analysis through 3D Modelling of Bronze Age Stone Moulds from Central Sardinia. *Minerals* **2021**, *11*, 1192. [[CrossRef](#)]
18. Casula, G.; Fais, S.; Cuccuru, F.; Bianchi, M.G.; Ligas, P. Diagnostic Process of an Ancient Colonnade Using 3D High-Resolution Models with Non-Invasive Multi Techniques. *Sensors* **2023**, *23*, 3098. [[CrossRef](#)] [[PubMed](#)]
19. Christaras, B.; Cuccuru, F.; Fais, S.; Papanikolaou, H. Application of Non Destructive Ultrasonic Techniques for the Analysis of the Conservation Status of Building Materials in Monumental Structures. In *Engineering Geology for Society and Territory-Volume 8*; Springer: Basel, Switzerland, 2015; Volume 8, pp. 139–143; ISBN 978-3-319-09408-3.
20. De Fino, M.; Galantucci, R.A.; Fatiguso, F. Condition Assessment of Heritage Buildings via Photogrammetry: A Scoping Review from the Perspective of Decision Makers. *Heritage* **2023**, *6*, 7031–7067. [[CrossRef](#)]
21. Dionsio, A.; Martinho, E.; Pozo-Antonio, J.S.; Sequeira Braga, M.A.; Mendes, M. Evaluation of Combined Effects of Real-Fire and Natural Environment in a Building Granite. *Constr. Build. Mater.* **2021**, *277*, 122327. [[CrossRef](#)]
22. Fais, S.; Casula, G.; Cuccuru, F.; Ligas, P.; Bianchi, M.G. An Innovative Methodology for the Non-Destructive Diagnosis of Architectural Elements of Ancient Historical Buildings. *Sci. Rep.* **2018**, *8*, 4334. [[CrossRef](#)] [[PubMed](#)]
23. Brunke, O.; Brockdorf, K.; Drews, S.; Muller, B.; Donath, T.; Herzen, J.; Beckmann, F. Comparison between X-Ray Tube-Based and Synchrotron Radiation-Based μ CT. In *Proceedings of the Developments in X-ray Tomography VI*, San Diego, CA, USA, 10–14 August 2008; Volume 7078, p. 70780U.
24. Kaufhold, A.; Halisch, M.; Zacher, G.; Kaufhold, S. X-Ray Computed Tomography Investigation of Structures in Opalinus Clay from Large-Scale to Small-Scale after Mechanical Testing. *Solid Earth* **2016**, *7*, 1171–1183. [[CrossRef](#)]
25. Wolanski, K.; Zarudzki, W.; Kiersnowski, H.; Dohnalik, M.; Drabik, K.; Urbaniec, A.; Skupio, R. X-Ray Computed Tomography (CT) Applied for Rock Core Analysis. *Bull. Russ. Acad. Nat. Sci.* **2017**, *5*, 43–50.
26. Omori, T.; Suzuki, S.; Michibayashi, K.; Okamoto, A. Super-Resolution of X-Ray CT Images of Rock Samples by Sparse Representation: Applications to the Complex Texture of Serpentine. *Sci. Rep.* **2023**, *13*, 6648. [[CrossRef](#)] [[PubMed](#)]
27. Albertin, F.; Bettuzzi, M.; Brancaccio, R.; Morigi, M.P.; Casali, F. X-ray Computed Tomography In Situ: An Opportunity for Museums and Restoration Laboratories. *Heritage* **2019**, *2*, 2028–2038. [[CrossRef](#)]
28. Albertin, F.; Morigi, M.P.; Bettuzzi, M.; Brancaccio, R.; Macchioni, N.; Saccuman, R.; Quarta, G.; Calcagnile, L.; Picchi, D. X-ray Tomography Unveils the Construction Technique of Un-Montu’s Egyptian Coffin (Early 26th Dynasty). *J. Imaging* **2022**, *8*, 39. [[CrossRef](#)]
29. Ashi, J. 11. Computed Tomography Scan Image Analysis of Sediments1. In *Proceedings of the Ocean Drilling Program, Scientific Results*; Texas A & M University: College Station, TX, USA, 1997; Volume 156, pp. 151–158.
30. Ujiie, K.; Maltman, A.J.; Sanchez-Gomez, M. Origin of Deformation Bands in Argillaceous Sediments at the Toe of the Nankai Accretionary Prism, Southwest Japan. *J. Struct. Geol.* **2004**, *26*, 221–231. [[CrossRef](#)]
31. Tonai, S.; Kubo, Y.; Tsang, M.-Y.; Bowden, S.; Ide, K.; Hirose, T.; Kamiya, N.; Yamamoto, Y.; Yang, K.; Yamada, Y.; et al. A New Method for Quality Control of Geological Cores by X-Ray Computed Tomography: Application in IODP Expedition 370. *Front. Earth Sci.* **2019**, *7*, 117. [[CrossRef](#)]
32. Martino, D.D.; Bellanova, M.; Cippo, E.P.; Felicetti, R.; Scherillo, A.; Kelleher, J.; Kis, Z.; Gorini, G. A Neutron Diffraction and Imaging Study of Ancient Iron Tie Rods. *J. Instrum.* **2018**, *13*, C05009. [[CrossRef](#)]
33. Mongy, T. Application of Neutron Tomography in Culture Heritage Research. *Appl. Radiat. Isot.* **2014**, *85*, 54–59. [[CrossRef](#)]
34. Bakirov, B.; Saprykina, I.; Kichanov, S.; Mimokhod, R.; Sudarev, N.; Kozlenko, D. Phase Composition and Its Spatial Distribution in Antique Copper Coins: Neutron Tomography and Diffraction Studies. *J. Imaging* **2021**, *7*, 129. [[CrossRef](#)]
35. Snaveley, N.; Seitz, S.M.; Szeliski, R. Modeling the World from Internet Photo Collections. *Int. J. Comput. Vis.* **2008**, *80*, 189–210. [[CrossRef](#)]

36. Westoby, M.J.; Brasington, J.; Glasser, N.F.; Hambrey, M.J.; Reynolds, J.M. 'Structure-from-Motion' Photogrammetry: A Low-Cost, Effective Tool for Geoscience Applications. *Geomorphology* **2012**, *179*, 300–314. [[CrossRef](#)]
37. Adamopoulos, E.; Rinaudo, F. Close-Range Sensing and Data Fusion for Built Heritage Inspection and Monitoring—A Review. *Remote Sens.* **2021**, *13*, 3936. [[CrossRef](#)]
38. Mestre-Runge, C.; Lorenzo-Lacruz, J.; Ortega-Mclear, A.; Garcia, C. An Optimized Workflow for Digital Surface Model Series Generation Based on Historical Aerial Images: Testing and Quality Assessment in the Beach-Dune System of Sa Ràpita-Es Trenc (Mallorca, Spain). *Remote Sens.* **2023**, *15*, 2044. [[CrossRef](#)]
39. Angelini, A.; Cozzolino, M.; Gabrielli, R.; Gentile, V.; Mauriello, P. Three-Dimensional Modeling and Non-Invasive Diagnosis of a Huge and Complex Heritage Building: The Patriarchal Basilica of Santa Maria Assunta in Aquileia (Udine, Italy). *Remote Sens.* **2023**, *15*, 2386. [[CrossRef](#)]
40. Assefa, S.; McCann, C.; Sothcott, J. Velocities of Compressional and Shear Waves in Limestones. *Geophys. Prospect.* **2003**, *51*, 1–13. [[CrossRef](#)]
41. Al-Dousari, M.; Garrouch, A.A.; Al-Omair, O. Investigating the Dependence of Shear Wave Velocity on Petrophysical Parameters. *J. Pet. Sci. Eng.* **2016**, *146*, 286–296. [[CrossRef](#)]
42. Casula, G.; Fais, S.; Cuccuru, F.; Bianchi, M.G.; Ligas, P.; Sitzia, A. Decay Detection in an Ancient Column with Combined Close-Range Photogrammetry (CRP) and Ultrasonic Tomography. *Minerals* **2021**, *11*, 1114. [[CrossRef](#)]
43. Kahraman, S.; Yeken, T. Determination of Physical Properties of Carbonate Rocks from P-Wave Velocity. *Bull. Eng. Geol. Environ.* **2008**, *67*, 277–281. [[CrossRef](#)]
44. Kassab, M.A.; Weller, A. Study on P-Wave and S-Wave Velocity in Dry and Wet Sandstones of Tushka Region, Egypt. *Egypt. J. Pet.* **2015**, *24*, 1–11. [[CrossRef](#)]
45. Pappalardo, G.; Mineo, S. Microstructural Controls on Physical and Mechanical Properties of Dolomite Rocks. *Rend. Online Della Soc. Geol. Ital.* **2016**, *41*, 321–324. [[CrossRef](#)]
46. Anselmetti, F.S.; Eberli, G.P. Sonic Velocity in Carbonate Sediments and Rocks. In *Carbonate Seismology*; Palaz, I., Marfurt, K.J., Eds.; Society of Exploration Geophysicists: Tulsa, OK, USA, 1997; pp. 53–74. ISBN 978-1-56080-038-5.
47. Eberli, G.P.; Baechle, G.T.; Anselmetti, F.S.; Incze, M.L. Factors Controlling Elastic Properties in Carbonate Sediments and Rocks. *Lead. Edge* **2003**, *22*, 654–660. [[CrossRef](#)]
48. Fais, S.; Ligas, P.; Cuccuru, F.; Maggio, E.; Plaisant, A.; Pettinau, A.; Casula, G.; Bianchi, M.G. Detailed Petrophysical and Geophysical Characterization of Core Samples from the Potential Caprock-Reservoir System in the Sulcis Coal Basin (Southwestern Sardinia–Italy). *Energy Procedia* **2015**, *76*, 503–511. [[CrossRef](#)]
49. Fais, S.; Cuccuru, F.; Casula, G.; Bianchi, M.G.; Ligas, P. Characterization of Rock Samples by A High-Resolution Multi-Technique Non-Invasive Approach. *Minerals* **2019**, *9*, 664. [[CrossRef](#)]
50. Soete, J.; Kleipool, L.M.; Claes, H.; Claes, S.; Hamaekers, H.; Kele, S.; Özkul, M.; Foubert, A.; Reijmer, J.J.G.; Swennen, R. Acoustic Properties in Travertines and Their Relation to Porosity and Pore Types. *Mar. Pet. Geol.* **2015**, *59*, 320–335. [[CrossRef](#)]
51. Weger, R.J.; Baechle, G.T.; Maserferro, J.L.; Eberli, G.P. Effects of Porestructure on Sonic Velocity in Carbonates. In Proceedings of the 2004 SEG Annual Meeting, Denver, CO, USA, 10–15 October 2004; pp. 1774–1777.
52. Cherchi, A. Appunti Biostratigrafici Sul Miocene Della Sardegna (Italia). *Mém. BRGM* **1974**, *78*, 433–445.
53. Gandolfi, R.; Porcu, A. Contributo Alla Conoscenza Delle Microfacies Mioceniche Delle Colline Di Cagliari (Sardegna). *Riv. Ital. Paleontol. Stratigr.* **1967**, *73*, 313–348.
54. Leone, F.; Pontillo, C.; Spano, C.; Carmignani, L.; Sassi, F.P. Benthic Paleocommunities of the Middle–Upper Miocene Lithostratigraphic Units from the Cagliari Hills (Southern Sardinia, Italy). In *Contribution to the Geology of Italy with Special Regard to the Paleozoic Basement. A Volume Dedicated to Tommaso Coccozza IGCP Project N° 276, Newsletter 5*; Carmignani, L., Sassi, F.P., Eds.; Pacini: Siena, Italy, 1992; Volume 5, pp. 151–158.
55. Cherchi, A.P. *Micropaleontological Researches in Sardinia: Guidebook*; Agip: Milano, Italy, 1985.
56. Barca, S.; Melis, E.; Annino, E.; Cincotti, F.; Ulzega, A.; Orrù, P.; Pintus, C. Note Illustrative Della Carta Geologica d'Italia Alla Scala 1: 50.000, Foglio 557, Cagliari. *Serv. Geol. D'Italia Carta Geol. D'Italia ISPRA.* **2005**, *1*, 240. [[CrossRef](#)]
57. Cuccuru, F.; Fais, S.; Ligas, P. Dynamic Elastic Characterization of Carbonate Rocks Used as Building Materials in the Historical City Centre of Cagliari (Italy). *Q. J. Eng. Geol. Hydrogeol.* **2014**, *47*, 259–266. [[CrossRef](#)]
58. Étienne, J. Technique d'imprégnation de Roches Par Des Résines Colorées Pour l'étude de La Porosité En Lame Mince. *Rev. L'Institut Fr. Pet. Ann. Combust. Liq.* **1963**, *18*, 611–619.
59. Lønøy, A. Making Sense of Carbonate Pore Systems. *AAPG Bull.* **2006**, *90*, 1381–1405. [[CrossRef](#)]
60. Katz, A.J.; Thompson, A.H. Quantitative Prediction of Permeability in Porous Rock. *Phys. Rev. B* **1986**, *34*, 8179–8181. [[CrossRef](#)] [[PubMed](#)]
61. Katz, A.J.; Thompson, A.H. Prediction of Rock Electrical Conductivity from Mercury Injection Measurements. *J. Geophys. Res.* **1987**, *92*, 599. [[CrossRef](#)]
62. Hager, J. Steam Drying of Porous Media. Ph.D. Thesis, Department of Chemical Engineering, Lund University, Lund, Sweden, 1998.
63. Semyonov, D. Agisoft Metashape Manual, LLC. St. Petersburg, Russia. Available online: https://www.agisoft.com/pdf/metashape_2_0_en.pdf (accessed on 27 February 2024).

64. ISRM. The Complete ISRM Suggested Methods for Rock Characterization, Testing and Monitoring: 1974–2006. In *Suggested Methods Prepared by the Commission on Testing Methods*; Ulusay, R., Hodson, J.A., Eds.; International Society for Rock Mechanics; ISRM Turkish National Group: Ankara, Turkey, 2007; p. 628; ISBN 975-93675-4-8.
65. ISRM. Upgraded ISRM Suggested Method for Determining Sound Velocity by Ultrasonic Pulse Transmission Technique. In *Testing and Monitoring: 2007–2014*; Ulusay, R., Ed.; ISRM: Cham, Switzerland; Heidelberg, Germany; New York, NY, USA; Dordrecht, The Netherlands; London, UK, 2014; pp. 95–99.
66. Casula, G.; Cuccuru, F.; Bianchi, M.G.; Fais, S.; Ligas, P. High Resolution 3-D Modelling of Cylinder Shape Bodies Applied to Ancient Columns of a Church. *Adv. Geosci.* **2020**, *54*, 119–127. [[CrossRef](#)]
67. Trampert, J.; Leveque, J.-J. Simultaneous Iterative Reconstruction Technique: Physical Interpretation Based on the Generalized Least Squares Solution. *J. Geophys. Res.* **1990**, *95*, 12553–12559. [[CrossRef](#)]
68. Mendes, M. A Hybrid Fast Algorithm for First Arrivals Tomography. *Geophys. Prospect.* **2009**, *57*, 803–809. [[CrossRef](#)]
69. Fais, S.; Casula, G. Application of Acoustic Techniques in the Evaluation of Heterogeneous Building Materials. *NDT E Int.* **2010**, *43*, 62–69. [[CrossRef](#)]
70. Lucia, F.J. Rock-Fabric/Petrophysical Classification of Carbonate Pore Space for Reservoir Characterization. *AAPG Bull.* **1995**, *79*, 1275–1300. [[CrossRef](#)]
71. Dunham, R.J. Classification of Carbonate Rocks According to Depositional Textures. *Am. Assoc. Pet. Geol.* **1962**, *1*, 108–121.
72. Choquette, P.W.; Pray, L.C. Geologic Nomenclature and Classification of Porosity in Sedimentary Carbonates. *Am. Assoc. Pet. Geol. Bull.* **1970**, *54*, 207–250.
73. Fais, S.; Cuccuru, F.; Ligas, P.; Casula, G.; Bianchi, M.G. Integrated Ultrasonic, Laser Scanning and Petrographical Characterisation of Carbonate Building Materials on an Architectural Structure of a Historic Building. *Bull. Eng. Geol. Environ.* **2017**, *76*, 71–84. [[CrossRef](#)]
74. Elkhrahy, I. 3D Structure from 2D Dimensional Images Using Structure from Motion Algorithms. *Sustainability* **2022**, *14*, 5399. [[CrossRef](#)]
75. Garia, S.; Pal, A.K.; Ravi, K.; Nair, A.M. A Comprehensive Analysis on the Relationships between Elastic Wave Velocities and Petrophysical Properties of Sedimentary Rocks Based on Laboratory Measurements. *J. Pet. Explor. Prod. Technol.* **2019**, *9*, 1869–1881. [[CrossRef](#)]
76. Verwer, K.; Braaksma, H.; Kenter, J.A. Acoustic Properties of Carbonates: Effects of Rock Texture and Implications for Fluid Substitution. *Geophysics* **2008**, *73*, B51–B65. [[CrossRef](#)]
77. Casula, G.; Fais, S.; Ligas, P. An Experimental Application of a 3D Terrestrial Laser Scanner and Acoustic Techniques in Assessing the Quality of the Stones Used in Monumental Structures. *Int. J. Microstruct. Mater. Prop.* **2009**, *4*, 45. [[CrossRef](#)]

Disclaimer/Publisher’s Note: The statements, opinions and data contained in all publications are solely those of the individual author(s) and contributor(s) and not of MDPI and/or the editor(s). MDPI and/or the editor(s) disclaim responsibility for any injury to people or property resulting from any ideas, methods, instructions or products referred to in the content.